Supporting Information

Electric-field jumps trigger a protein response preceeding the ultrafast photoisomerization

Clark Zahn,[1] Florian Nikolas Brünig,[1] Till Stensitzki,[1] Shane Carlson, [1] Florian Bartonitz,[1] Philipp Alt, [3] Jonathan R. Church, [2] Rolf Diller,[3] Ramona Schlesinger, [1] Roland Rüdiger Netz,[1] Igor Schapiro,[2] Karsten Heyne[1]*

[1] Freie Universität Berlin, Department of Physics, Arnimallee 14, 14195 Berlin, Germany[3]

[2] Fritz Haber Center for Molecular Dynamics Research, Institute of Chemistry, The Hebrew University of Jerusalem, Jerusalem, 91904, Israel

[3] Rheinland-Pfälzische Technische Universität Kaiserslautern-Landau, Department of Physics, Erwin-Schrödinger-Straße 46, 67663 Kaiserslautern, Germany

Content:

1 Understanding Dynamic Electric Field Screening via a Fit of the Water Absorption Spectrum

The time-dependent electric susceptibility $\widetilde{\chi}(t)$ is the linear response function that gives the polarization $\boldsymbol{P}(t)$ of a medium in response to an applied electric field $\boldsymbol{E}(t)$. In an isotropic medium, $\widetilde{\chi}(t) \mapsto \mathbb{R}$ and

$$\boldsymbol{P}(t) = \varepsilon_0 \int_0^t \mathrm{d}t' \, \widetilde{\chi}(t-t')\boldsymbol{E}(t') \,, \tag{1}$$

where ε_0 is the vacuum permittivity. Let $X(t)$ denote the running integral of the response function,

$$X(t) \equiv \int_0^t \mathrm{d}t' \, \widetilde{\chi}(t') \,. \tag{2}$$

Comparison of Eqs. (1) and (2) reveals that $X(t)$ gives the polarization in response to a constant applied electric field switched on at $t = 0$. The positive-domain Fourier transform of $\widetilde{\chi}(t)$ gives the frequency-dependent electric susceptibility,

$$\int_0^\infty \mathrm{d}t \, e^{-i\omega t}\widetilde{\chi}(t) = \chi(\omega) = \chi'(\omega) - i\chi''(\omega) \,, \tag{3}$$

where $\chi'(\omega)$ is the real (refractive or dispersive) part and $\chi''(\omega)$ is the imaginary (dissipative or absorptive) part.

1.1 Fitting Function

We seek to fit an experimental spectrum $\chi(\omega)$ (both real and imaginary parts) with a linear combination of several damped harmonic oscillator response functions, Gaussian/Dawson integral response functions, and a real constant. The damped harmonic oscillator response function has the form,

$$\chi_{\mathrm{DHO}}(\omega) = \frac{1}{k - m\omega^2 + i\gamma\omega} \,. \tag{4}$$

This can be Fourier transformed to get the correlation function in the time domain,

$$\widetilde{\chi}_{\mathrm{DHO}}(\tau) = \frac{1}{m\omega_1} e^{-\frac{1}{2}\gamma\tau} \sin\omega_1\tau \,, \tag{5}$$

where ω_1 is the natural damped frequency,

$$\omega_1 = \sqrt{\omega_0^2 - \frac{\gamma^2}{4}} \,, \tag{6}$$

and can be either real or imaginary. The Gaussian/Dawson response function is taken here to have a Gaussian shape in the positive-ω domain of its imaginary part,

$$\chi''_{\mathrm{G}}(\omega) = Ae^{-\frac{1}{2}\frac{(\omega-\mu)^2}{\sigma^2}} \,, \quad \omega > 0 \,. \tag{7}$$

It is assumed that the response function is antisymmetric, thus, $\chi''_{\mathrm{G}}(\omega) = -\chi''_{\mathrm{G}}(-\omega)$. The result of using the Kramers Kronig relation, i.e., of taking the Hilbert transform of the imaginary part, gives for the real part

$$\chi'_{\mathrm{G}}(\omega) = \frac{2A}{\sqrt{\pi}} \left(F\left(\frac{\omega-\mu}{\sqrt{2}\sigma}\right) + F\left(\frac{-\omega-\mu}{\sqrt{2}\sigma}\right)\right) \tag{8}$$

$$\approx \frac{2A}{\sqrt{\pi}} F\left(\frac{\omega-\mu}{\sqrt{2}\sigma}\right) \,, \tag{9}$$

where $F(x)$ is the Dawson integral

$$F(x) = e^{-x^2} \int_0^x \mathrm{d}t \, e^{-t^2} \,. \tag{10}$$

Note that this results in a jump discontinuity at $\omega = 0$. For narrow peaks at higher frequencies, the fast decay of the Gaussian means that this discontinuity is very small. The Gaussian is chosen to fit some features because the fat tails in the imaginary part of the damped harmonic oscillator make it difficult to fit some modes. The Gaussian/Dawson can be Fourier transformed to get the correlation function in the time domain,

$$\widetilde{\chi}_{\mathrm{G}}(\tau) = \frac{A\sigma}{\sqrt{2\pi}} e^{-\frac{1}{2}\sigma^2\tau^2} \mathrm{Im}\left\{ e^{-i\mu\tau} \left(1 + \mathrm{erf}\left(\frac{\mu + i\sigma^2\tau}{\sqrt{2}\sigma}\right)\right)\right\} \,, \tag{11}$$

where $\mathrm{erf}(x)$ is the error function. Finally, the fitting function for $\chi(\omega)$ should include a real-valued constant, which represents the optical susceptiblity, $R = \chi(\omega \to \infty)$. The fit is carried out on the real and imaginary parts of $\chi(\omega)$ simultaneously and with equal weight. Because the data is plotted on a log scale, the log of the data is fit with the log of the fitting function. The fit comprises a minimization of the sum of squares of the residuals, i.e., a least-squares fit.

1.2 Fit to Experimental Water Susceptibility

The fitted data is a compiled experimental spectrum of bulk liquid water measured at or near 300 K, extending over the frequency range of $\nu \approx 100$ MHz to $\nu \approx 150$ THz. The data was compiled from the original sources, Refs. [1, 2, 3, 4, 5], in Ref. [6], which also refers to Ref. [7]. See the Supplementary Information of Ref. [6] for detailed information.

In all, five damped harmonic oscillators and three Gaussians are fit to the data. The fit is shown in Fig. 1**(a–d)**, plotted over the frequency $\nu = \omega/2\pi$, along with each of the Gaussian and damped harmonic oscillator response functions, and R. The respective real parts are shown in panel **(a)**, and the imaginary parts in panel **(b)**. The Gaussian response functions are labeled in the legend with an asterisk. Note that the Debye peak at $\nu \approx 20$

GHz is fitted with a damped harmonic oscillator, instead of the actual Debye function, because the latter choice results in a fit that is too high in the IR regime. The resulting fit parameters are collected together in Table 1. Fig. 1**(c)** shows the time-dependent response function $\widetilde{\chi}(t)$ (see Eq. (1)) in lin-log. The running integral $X(t)$ (see Eq. (2)) is calculated numerically and plotted in Fig. 1**(d)**.

Fig. 1**(e–h)** groups the fitted damped harmonic oscillators and Gaussian functions from the fit shown in Fig. 1**(a–d)** into three sums of terms: Debye (one damped harmonic oscillator only), intermolecular vibrations (including the intermediate Gaussian at $\nu \approx 40$ THz), and intramolecular vibrations. In the inset of Fig. 1**(h)**, the running integral $X(t)$ is plotted in lin-log. This illustrates clearly how the Debye response underpins more than 90% of the static susceptibility of water ($X(t \to \infty)$ or $\chi(\omega \to 0)$), and how, for short times, the susceptibility is very small. Thus, at short timescales, where the response is dominated by vibrational modes, water is rather transparent to electric fields.

A version of the main panel of Fig. 1**(h)** is reproduced as the right inset of Fig. 3(b) of the main text.

ν_0 [THz]	m [THz^{-2}]	γ [THz^{-1}]
0.968	$3.737 \cdot 10^{-4}$	$1.159 \cdot 10^{-1}$
3.480	$1.078 \cdot 10^{-3}$	$3.360 \cdot 10^{-1}$
5.290	$5.059 \cdot 10^{-4}$	$1.959 \cdot 10^{-2}$
49.199	$7.256 \cdot 10^{-4}$	$9.392 \cdot 10^{-3}$
64.578	$1.554 \cdot 10^{-3}$	$8.784 \cdot 10^{-2}$
$\mu/2\pi$ [THz]	σ [THz]	A [unitless]
16.836	35.581	1.039
40.064	34.722	0.060
99.711	30.987	0.687
R [unitless]		
0.7662		

Table 1: Fit parameters for the fit shown in Fig. 1. Note: $\nu_0 = k/m$ for the damped harmonic oscillators.

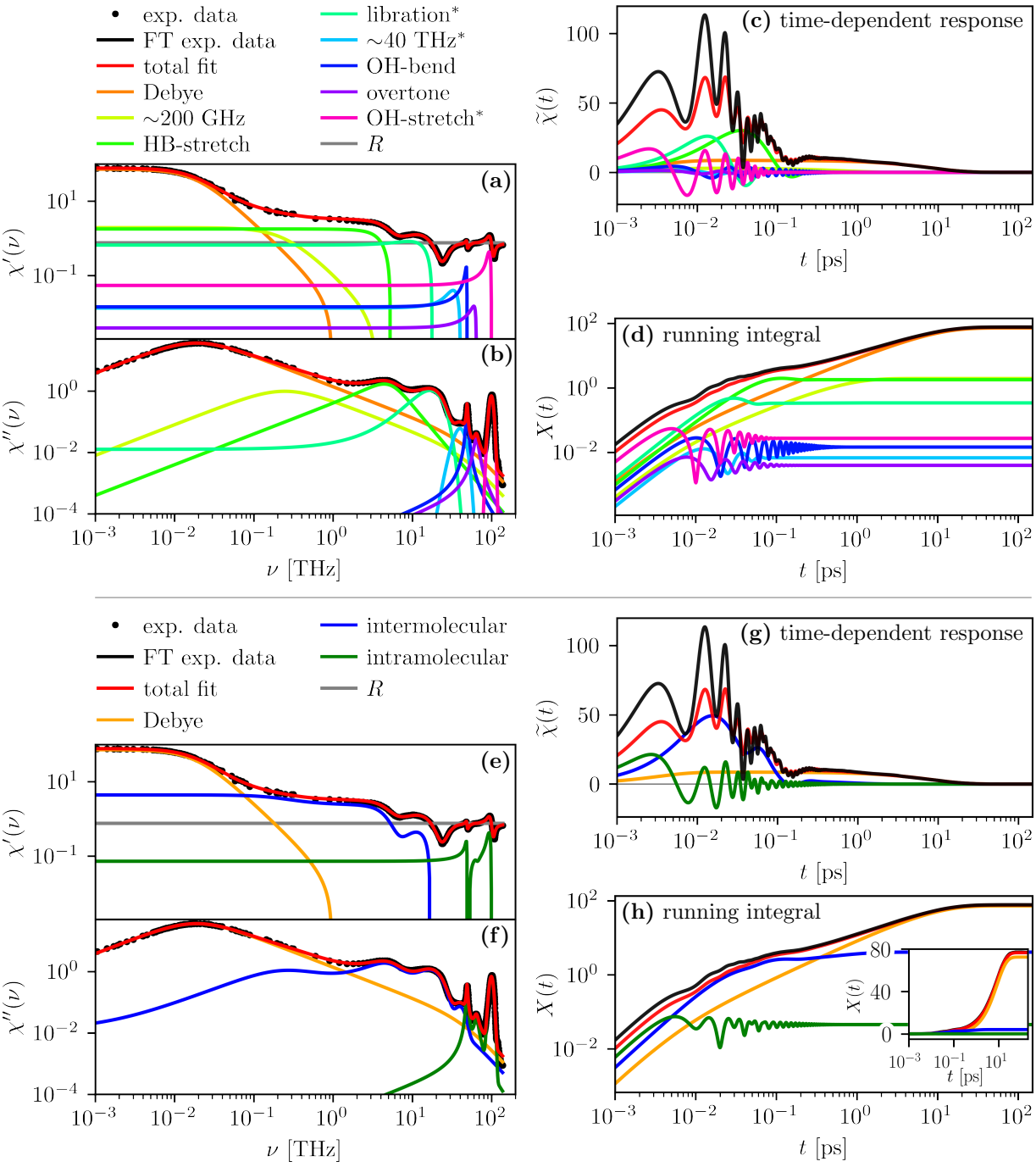

Figure 1: Fit of the experimental frequency-dependent electric susceptibility $\chi(\nu)$ for water at 300 K. **(a–d)** show the fit with a full decomposition into damped-harmonic and Gaussian terms. **(a)**, **(b)** Real and imaginary parts of the fit, respectively, compared to the fitted experimental data, along with each individual term comprising the fitting function. **(c)** The Fourier transform of the data in (a) and (b), which gives the time-dependent response function $\widetilde{\chi}(t)$ (see Eq. (1)). **(d)** The running integral $X(t)$ (see Eq. (2)) of the data in (c), which gives the response to an electric field jump, i.e., a constant electric field that is switched on at $t = 0$. **(e–h)** Show the same data as (a–d), but with the respective damped-harmonic and Gaussian terms summed into Debye and inter- and intramolecular vibrational contributions. Here, the intermediate Gaussian at $\nu \approx 40$ THz is grouped together with the intermolecular vibrational contribution. The inset in (h) shows the same data as in (h) in lin-log, which illustrates how the Debye mode dominates the response.

2 Additional QM/MM simulation results

The simulation results of the excited state dynamics simulations are summarized in the following for the five different quantum mechanical (QM) partitionings with names in brackets. The smallest QM region contains only the retinal with a total charge of +1 e due to the protonated Schiff base (Ret). The second setup additionally comprises the deprotonated Asp85 and Asp212 residues and the three water molecules in their vicinity, amounting to a charge of −1 e (Ret + 2Asp + $3H_2O$). The third QM region also contains the protonated Arg82 residue and the two closest water molecules to complete the quadrupol counter ion complex near the retinal Schiff base with a total neutral charge (Ret + CI complex). Two additional setups four and five are copies of setups one and three but including additionally the Trp86 and Trp182 residues. The smaller one is setup four consisting of retinal and the Trp residues (Ret + 2Trp). The largest QM system five includes the retinal, the two Trp residues, the deprotonated Asp85 and Asp212 residues, the protonated Arg82 residue, and the five closest water molecules to the retinal (Ret + 2Trp + CI complex).

In Fig. 2 the numbering of the dihedral angles along the retinal backbone is illustrated together with an illustration of the typical conformational transition during isomerization. Dihedral angle 7 is the most relevant reaction coordinate, which is seen in Fig. 3, where the dynamics of all retinal dihedral angles across all simulations are shown together. In Fig. 4A-E the dynamics of the dihedral angle 7 of the retinal chromophore is summarized for each type of QM system. The vertical lines in Fig. 3 and Fig. 4 indicate times of surface hopping events in the hh-TDA simulations. Surface-hopping is most likely to occur near the conical intersection between the ground and excited state potential energy surfaces, which is located at a dihedral angle of approximately 90°. The general trend across all simulation results is a fast isomerization of the retinal chromophore within about 100 fs from an initial dihedral angle of approximately 0° to a dihedral angle of approximately 90°. The dihedral angle fluctuates around this value until a surface hopping event occurs. Subsequently, the isomerization proceeds to the all-trans state indicated by a dihedral angle of 180° or returns to the initial state close to 0°. In contrast to the other systems, for the two smallest QM regions including only the retinal and additionally the adjacent Trp86 and Trp182 residues, the isomerization is not completed within the simulated times of up to 500 fs (see Fig. 4A and D). This is probably related to the rare observation of surface hopping events for these systems, indicating that the energy gap between the ground and excited state potential energy surfaces remains too large. This may stem from steric hindrance of the retinal to reach the conical intersection

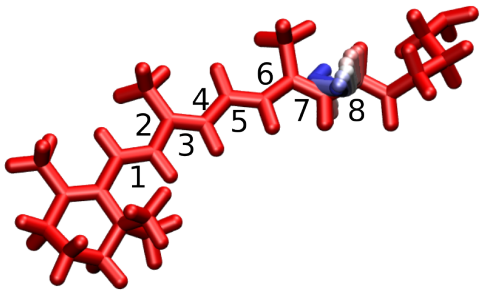

Figure 2: Illustration of the dihedral angles along the retinal backbone. The relevant reaction coordinate is angle 7 which captures well the typical conformational transition as illustrated by snapshots forward in time from red to blue. See Fig. 3 for simulation trajectories of the various dihedrals.

or from the absence of the counter-ion complex near the Schiff base as a polarizable medium.

In Fig. 4D-F the dipole moment trajectories of the QM regions of all simulations are shown. Data is again presented for the different QM regions in the five different panels. For each simulation the dipole-moment trajectory is shown in blue as projected on the average dipole moment of the retinal from which the effective difference field was calculated as described in the Methods section. The thick blue solid line is the average across all simulations. The dipole moment magnitude orthogonal to the average dipole moment of the retinal is shown for all simulations as orange solid lines, the average is given as a thick orange solid line. Importantly, these dipole moment trajectories are exactly the data that is used to calculate the projected infrared absorption spectra in EDF2. One sees that throughout the simulations the dipole moment magnitude is strongest during the initial 50 fs and strongly fluctuates around a value of about 10 D to 20 D. This is before significant isomerization of the retinal chromophore occurs when comparing to the data in Fig. 4A-E. The dipole moment magnitude appears generally increased for the larger QM systems, i.e. upon inclusion of the deprotonated Asp85 and Asp212 residues and three two closest water molecules, indicating that the counter-ion complex near the Schiff base constructively contributes to the dipole moment of the retinal chromophore. The inclusion of the Trp86 and Trp182 residues in the QM region on the other hand appears to have the opposite effect on the dipole moment magnitudes, which are slightly smaller.

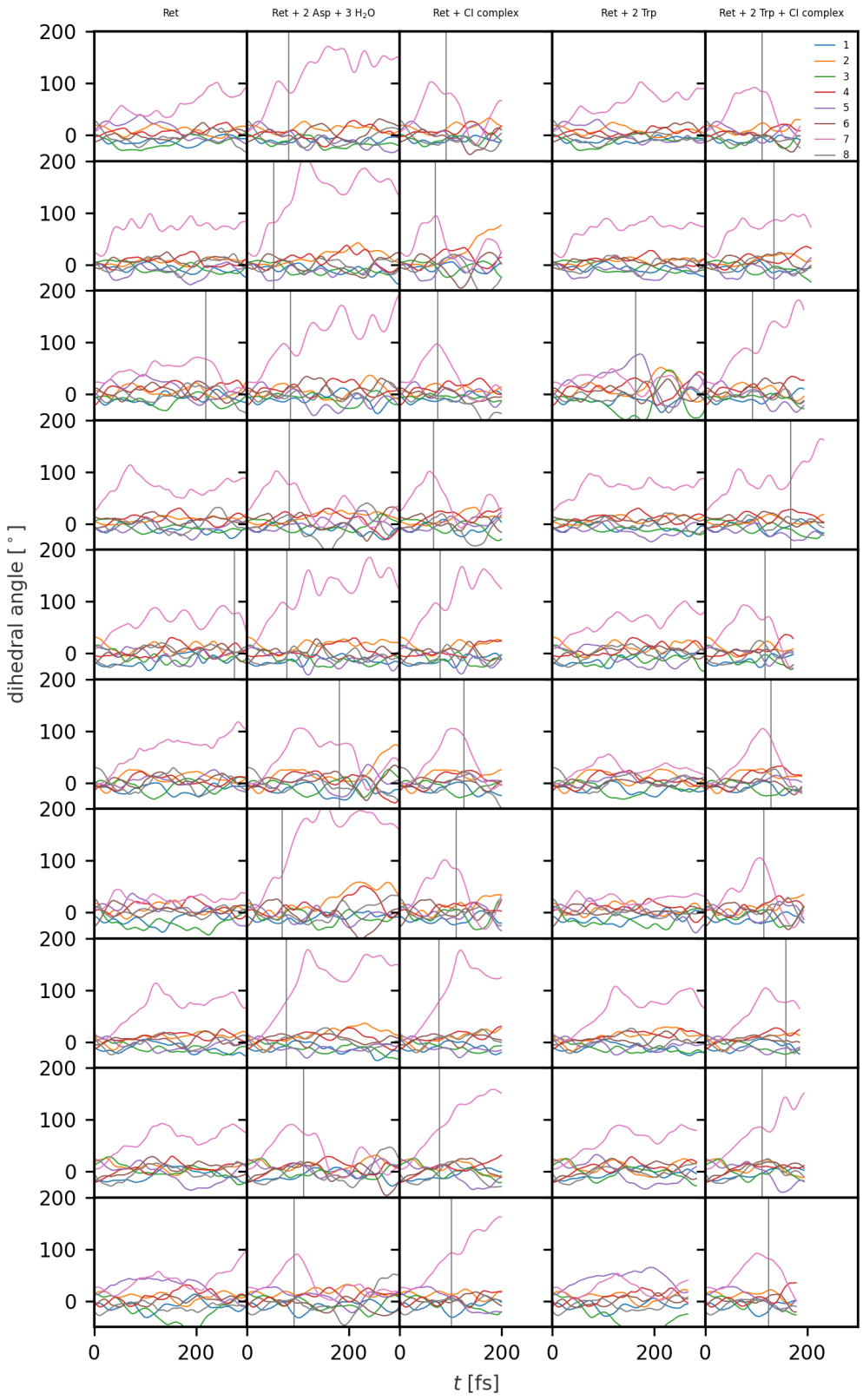

Figure 3: Dihedral angle dynamics of the retinal chromophore as a function of time for all QM regions and all simulation runs. Each color represents a different dihedral angle along the retinal backbone.

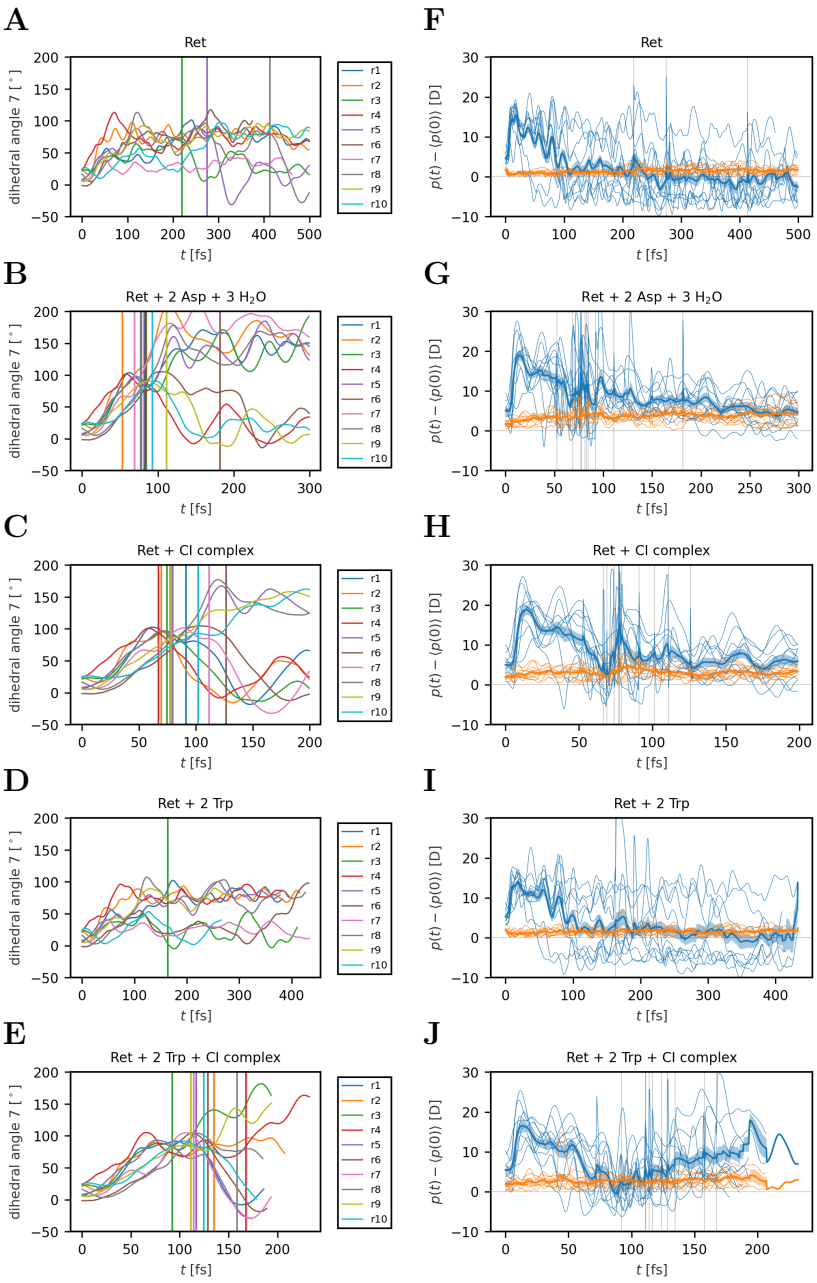

Figure 4: Simulation results for the excited state dynamics of the retinal chromophore in bacteriorhodopsin for the five different QM regions denoted in the title of each figure. A-E: Dihedral angle dynamics of the retinal chromophore as a function of time. Each line shows a different trajectory. F-J: Dipole moment trajectories of the QM regions projected on the axis of the average dipole moment as defined in the Methods section are shown as blue solid lines for the different simulations. Dipole moment magnitudes in the orthogonal plane are given as orange solid lines. The vertical lines show times of the surface hopping events in the hh-TDA simulations.

References

[1] H. D. Downing and D. Williams, J. Geophys. Res. **80**, 1656 (1975).

[2] H. P. Schwan, R. J. Sheppard, and E. H. Grant, J. Chem. Phys. **64**, 2257 (1976).

[3] U. Kaatze, J. Chem. Eng. Data **34**, 371 (1989).

[4] Z. Czumaj, Mol. Phys. **69**, 787 (1990).

[5] J. Barthel, K. Bachhuber, R. Buchner, H. Hetzenauer, and M. Kleebauer, Ber. Bunsenges. Phys. Chem. **95**, 853 (1991).

[6] S. Carlson, F. N. Brünig, P. Loche, D. J. Bonthuis, and R. R. Netz, J. Phys. Chem. A **124**, 5599 (2020).

[7] W. Ellison, J. Phys. Chem. Ref. Data **36**, 1 (2007).

3. Normal-Mode Analysis of retinal embedded in the protein

The ground state vibrational frequencies of the retinal protonated Schiff base in bacteriorhodopsin (bR) were calculated for the resting state (PDB: 7Z0a) and its K-intermediate (PDB: 1M0K). Normal-node analysis with the hybrid quantum mechanics/molecular mechanics (QM/MM) method was used as implemented in Orca v5.0.3. The retinal chromophore and sidechain of the lysine were part of the QM region. The QM-MM boundary was placed at the C_α-C_β bond of the lysine. The remaining protein comprised the MM region and was described by the Amber ff14SB force field. The QM region was treated at the B3LYP/Def2-SVP level of theory with a D4 dispersion correction. The interactions between the QM and MM regions were treated with electrostatic embedding. Amino acid sidechain residues with at least one atom within 5 Å of the QM region were allowed to relax during the initial optimization. The optimized structures were then used in the subsequent normal-mode analysis calculations.

Table 1. Vibrational Frequencies obtained from normal mode analysis for bacteriorhodopsin and the K-intermediate in inverse wavenumbers (cm^{-1}) calculated using B3LYP/Def2-SVP with a D4 dispersion correction and treating the MM region with the Amber ff14SB force field.

all-*trans* (7Z0a)					**13-*cis* (1M0K)**				
44.86	547.1	1045.69	1393.9	3036.77	37.17	542.67	1033.31	1381.16	3028.3
72.04	570.87	1050.35	1397.67	3037.84	64.92	562.11	1045.13	1385.47	3030.34
85.4	581.86	1067.28	1403.51	3040.77	74.77	579.72	1050.53	1392.22	3038.29
103.95	619.01	1086.16	1406.49	3040.9	100.96	586.24	1067.42	1403.18	3039.85
108.39	635.95	1091.08	1420.99	3044.92	108.95	601.16	1071.33	1405.88	3042.93
131.03	660.6	1111.82	1427.74	3053.63	134.53	644.93	1081.73	1412.09	3047.18
145.93	668.09	1132.88	1430.94	3061.98	135.32	672.77	1111.51	1421.25	3060.1
157.18	706.42	1157.63	1436.18	3062.67	147.06	706.41	1132.76	1433.69	3060.43
164.36	741.71	1165.95	1438.73	3080.94	155.62	713.37	1157.78	1438.92	3068.42
176.94	786.5	1199.58	1442.12	3082.52	173.59	721.76	1160.79	1445.84	3080.54
192.2	827.49	1206.65	1448.88	3089.16	182.77	756.6	1198.27	1448.98	3081.15
204.52	847.48	1212.68	1450.59	3092.96	193.86	825.37	1208.82	1451.35	3083.32
225.82	860.35	1220.31	1452.2	3100.11	200.49	845.66	1210.24	1454.64	3086.57
233.49	871.38	1228.62	1458.03	3108.48	218.22	849.41	1218.47	1459.0	3090.57
242.88	880.58	1236.82	1459.33	3109.96	224.56	860.94	1220.1	1459.47	3094.68
260.46	884.23	1247.03	1463.43	3117.09	231.13	865.09	1231.74	1465.47	3097.92
270.11	888.3	1248.57	1465.03	3129.11	244.63	871.31	1239.49	1468.08	3112.11
278.57	896.53	1266.49	1468.4	3131.22	260.5	883.24	1253.19	1472.39	3123.67
300.89	905.76	1278.37	1475.35	3134.97	261.4	899.92	1262.45	1473.84	3128.64
312.07	913.78	1287.54	1476.46	3135.9	284.9	905.4	1285.35	1477.78	3129.91
319.54	927.48	1288.28	1480.75	3149.09	315.42	910.09	1285.92	1479.28	3142.01
335.87	934.19	1302.2	1482.53	3149.59	327.87	926.4	1291.38	1480.29	3156.53
356.22	936.91	1307.11	1487.3	3157.99	336.65	935.08	1300.72	1483.29	3158.79
380.6	952.93	1328.35	1496.13	3160.54	361.79	936.2	1312.48	1489.8	3161.65
393.22	969.3	1332.71	1509.52	3167.35	385.54	951.0	1322.05	1491.61	3162.92
404.0	985.74	1340.51	1597.21	3168.79	391.64	959.54	1327.64	1492.11	3170.23
407.38	987.33	1352.71	1611.41	3169.54	398.02	970.57	1329.95	1581.78	3170.43
419.02	995.03	1359.93	1643.29	3171.86	406.02	985.29	1345.03	1590.12	3175.69
432.04	997.72	1364.08	1662.5	3185.79	424.45	988.77	1350.78	1626.01	3187.2
460.32	1003.72	1370.1	1674.62	3190.66	457.4	991.16	1354.98	1642.98	3196.03
463.4	1010.1	1373.43	1717.86	3211.14	463.14	994.53	1361.94	1661.55	3208.58
495.45	1012.58	1377.96	3009.33	3215.52	478.38	1007.58	1371.48	1683.33	3220.44
506.47	1026.18	1378.8	3022.38	3225.45	496.72	1011.62	1376.67	3004.41	3221.58
519.91	1034.16	1381.79	3029.27	3406.86	510.71	1015.91	1377.75	3022.42	3229.41
530.65	1042.12	1387.47	3035.12		521.83	1022.7	1379.4	3024.21	3541.65